Pillar Height Dependence of Field-Emission Properties in an Array of Carbon Nanotube Pillars

2013 Jpn. J. Appl. Phys. 52 085101

(http://iopscience.iop.org/1347-4065/52/8R/085101)

Japanese Journal of Applied Physics **52** (2013) 085101 **REGULAR PAPER**
http://dx.doi.org/**10.7567/JJAP.52.085101**

Pillar Height Dependence of Field-Emission Properties in an Array of Carbon Nanotube Pillars

Chia-Tsung Chang[1]*, Chuan-Ping Juan[2], and Huang-Chung Cheng[1]

[1]*Department of Electronics Engineering and Institute of Electronics, National Chiao Tung University, Hsinchu 300, Taiwan, R.O.C.*
[2]*Department of Electronics Engineering, St. John's University, New Taipei City 25135, Taiwan, R.O.C.*
E-mail: bgi815.ee96g@g2.nctu.edu.tw

Received October 8, 2012; accepted May 23, 2013; published online July 23, 2013

Carbon nanotube pillars with optimal field-emission properties, including a high field enhancement factor β of 5384 and a low turn-on field E_{to} of 0.84 V/μm, have been achieved when the ratio of interpillar spacing to pillar height is 2. However, when this ratio exceeds 2, the field enhancement factor increases with increasing pillar height since the field can be enhanced by increasing the aspect ratio. When the ratio is smaller than 2, the field enhancement factor decreases with increasing pillar height owing to the increased field-screening effect. A simulation has been performed to verify the experimental results. © 2013 The Japan Society of Applied Physics

1. Introduction

Carbon nanotubes (CNTs) have attracted a great deal of attention as an electron-emitting material owing to their high aspect ratio, high mechanical strength, chemical inertness, large current capability, and high thermal conductivity. In general, the field enhancement factor for an individual CNT is considered to be better than that for CNT films because the electric field in one tube in a CNT film is screened by the proximity of its neighboring tubes.[1)] The effects of the CNT diameter, length, intertube distance, and density of a CNT film on field enhancement factors have been investigated in previous studies.[2–11)] For an individual CNT, the longest vertically aligned CNT with the smallest radius is ideal for electron emission. On the other hand, the optimal ratio of intertube distance to CNT height for CNT films was reported by Nilsson et al.[3)] to be 2 for field-emission (FE) characteristics. Moreover, the FE characteristics of a CNT film should be enhanced with increasing CNT height when the CNT is short.[7)] As is well known, it is very difficult to grow a very long vertically aligned CNT and to accurately control the intertube distance for CNT films. However, CNT films are generally used for practical purposes, implying that it is very difficult to empirically examine the effects of the ratio of intertube distance to CNT height on the FE characteristics of CNT films because the length and intertube distance of a CNT are inaccurately known. Since the van der Waals interactions between CNTs are strong, long vertically aligned tubes can be achieved using their pillarlike structures. Moreover, the ratio of interpillar spacing R to pillar height H for CNT pillars can be properly controlled to attain the optimal FE characteristics for practical purposes. In recent years, CNT pillars have been widely adopted for FE devices.[12–21)] However, systematic experiments to determine the optimal conditions by changing H at a fixed R were not conducted.[20,21)] In this letter, we report that the pillar structures of CNTs with optimal FE properties can be found at an R/H ratio of 2 when R is fixed at 30 μm. A computer simulation was conducted to verify and investigate the FE results.

2. Experimental Procedure

First, a 4-in. (100) p-type wafer is cleaned by the standard RCA cleaning process. A catalytic layer is then deposited and defined via the lift-off process. 10-nm-thick aluminum (Al), 1-nm-thick titanium (Ti), and 4-nm-thick codeposited cobalt–titanium (Co–Ti) layers, respectively serving as the barrier, adhesion, and catalytic layers, are sequentially deposited at room temperature on the Si substrate using a magnetron sputtering system (Ion Tech Microvac 450CB). The Al layer serves to increase the surface roughness and the planar density of catalyst particles in order to obtain an excellent profile and a high density of CNTs. The codeposited Co–Ti layer suppresses the coalescence of Co nanoparticles in order to obtain uniformly distributed CNT pillars.[22)] The diameter and interpillar spacing of CNT pillars are set to 50 and 30 μm, respectively. Finally, CNT pillars are grown on a patterned catalyst by thermal CVD. The two-step synthesis procedure involving the pretreatment and growth processes is shown in Fig. 1. The catalyst metal is pretreated with hydrogen at 600 °C for 5 min under a flow of 300 sccm to produce nanoparticles.[23)] Then, CNTs are grown at 700 °C under hydrogen, nitrogen, and ethylene flow rates of 300, 500, and 100 sccm, respectively. The height of CNT pillars is controlled to be 5, 10, 15, 30, and 60 μm, accordingly, by adjusting the synthesis time.

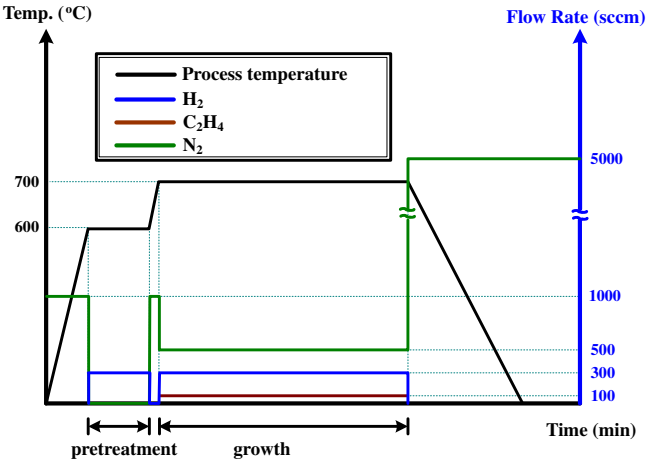

Fig. 1. (Color online) Growth process for CNT pillars.

The morphologies and microstructures of CNT pillars are characterized by field-emission scanning electron microscopy (FE-SEM; Hitachi S-4700I) and high-resolution transmission electron microscopy (HRTEM; TECNAI 20), respectively.

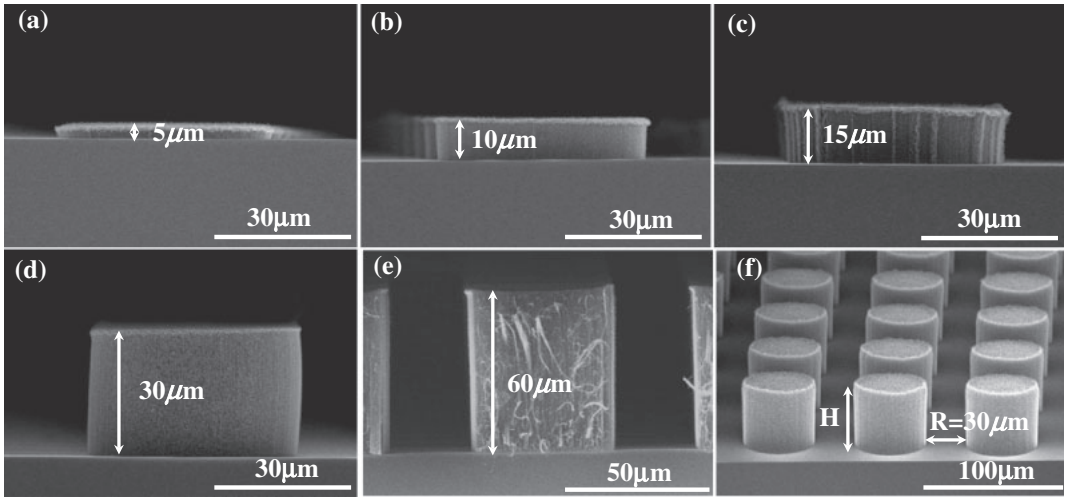

Fig. 2. FE-SEM images of CNT pillars with heights of (a) 5, (b) 10, (c) 15, (d) 30, and (e) 60 μm; (f) 45° tilted view of CNT pillar array.

When performing the measurement, the device is loaded into a high-vacuum chamber and the pressure is controlled at 8×10^{-6} Torr. An anode voltage is applied with a source measurement unit (Keithley 237) and the cathode is biased at 0 V (Keithley 238). A distance of 300 μm is maintained between the anode and the tip of CNT pillars.

A simulation is carried out using commercial software (ISE-TCAD) to verify the experiment results. The carrier density is computed from the Boltzmann statistics. To further link the carrier density to the electrostatic field in CNT pillars, the transport equations are solved together with Poisson's equation. The FE characteristic is modeled by the Fowler–Nordheim (FN) equation.

3. Results and Discussion

Cross-sectional FE-SEM images of CNTs of different pillar heights are shown in Figs. 2(a)–2(e). As can be seen, the pillar height can be controlled precisely by adjusting the growth time. In Fig. 2(f), the FE-SEM image (45° tilted view) of the CNT pillar array exhibits long vertically aligned CNTs. Figure 3 shows an HRTEM image of an individual CNT in the pillars, revealing a closed tip and a multiwalled structure consisting of graphite sheets aligned parallel to the tube axis. The outer diameter of an individual CNT is measured to be about 16 nm.

Plots of the emission current density J as a function of the macroscopic field E_m for CNT pillars of different heights are shown in Fig. 4(a). As can be seen, the current density–electric field curves are relatively smooth. The turn-on field (E_{to}) and threshold field (E_{th}) extracted from Table I are 10 μA/cm^2 and 10 mA/cm^2, respectively. Clearly, the lowest turn-on field and threshold field are 0.84 and 1.51 V/μm, respectively, for a pillar height of 15 μm. Furthermore, the FE data are analyzed using the FN model for these five different pillar heights, as shown in Fig. 4(b). The maximum slope, indicating the highest enhancement factor, is also obtained for a pillar height of 15 μm.

To verify the experimental results, the electrostatic field distribution and FE characteristics of the CNT pillars are examined by computer simulation. The electrostatic field distributions of CNTs of different pillar heights at the applied voltage of 600 V are then calculated and shown in Fig. 5. To extract the field enhancement factor from the slope of the FN plot, we try to simplify the simulation modeling. First, a single CNT pillar comprising many CNTs was compared with a single CNT solid pillar. We find that the electrostatic field distributions and electrostatic potential distributions of both structures are similar. Therefore, the modeling of CNT solid pillars is adopted in the simulation. The dimensions of the pillar arrays for the simulation are the same as those for the experiment. For simplicity, the number of pillars employed for the simulation is set to five since the contour of the electrostatic fields at the pillar edges, marked by dashed dots in Fig. 5, seem to be flat at the central pillar. These five pillars are then denoted as "Left Outer" (LO), "Left Middle" (LM), "Center" (C), "Right Middle" (RM), and "Right Outer" (RO). Furthermore, the electrostatic fields at the right and left edges of the RO pillar are respectively named $E_{pE,RO\text{-}R}$ and $E_{pE,RO\text{-}L}$, as indicated in Fig. 5, for example. When the pillar height is 5 μm, the electrostatic fields at the pillar edges are relatively higher than those in the interior for all five pillars. The electrostatic fields in the interior of the pillars are almost zero because the field-screening effect is induced by the high density of CNTs

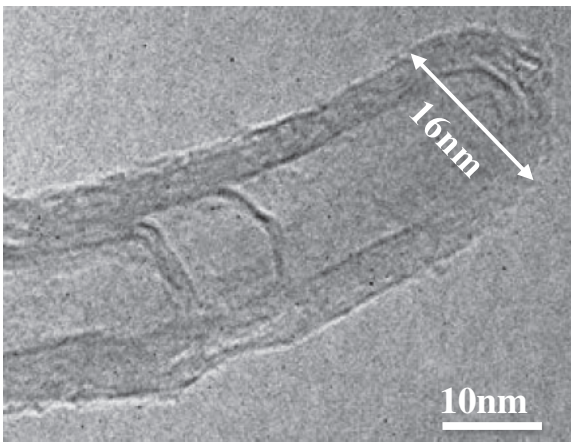

Fig. 3. HRTEM image of individual CNT in CNT pillars.

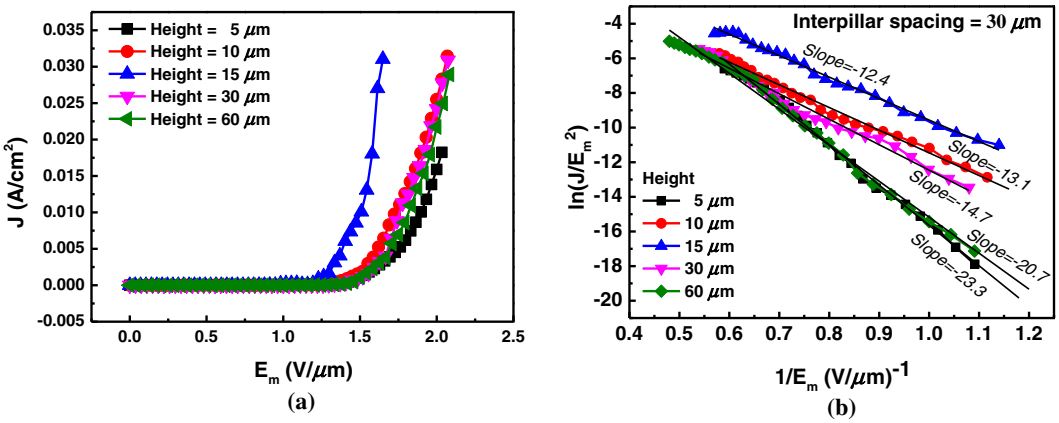

Fig. 4. (Color online) (a) J–E_{app} curves and (b) FN plots for five different pillar heights.

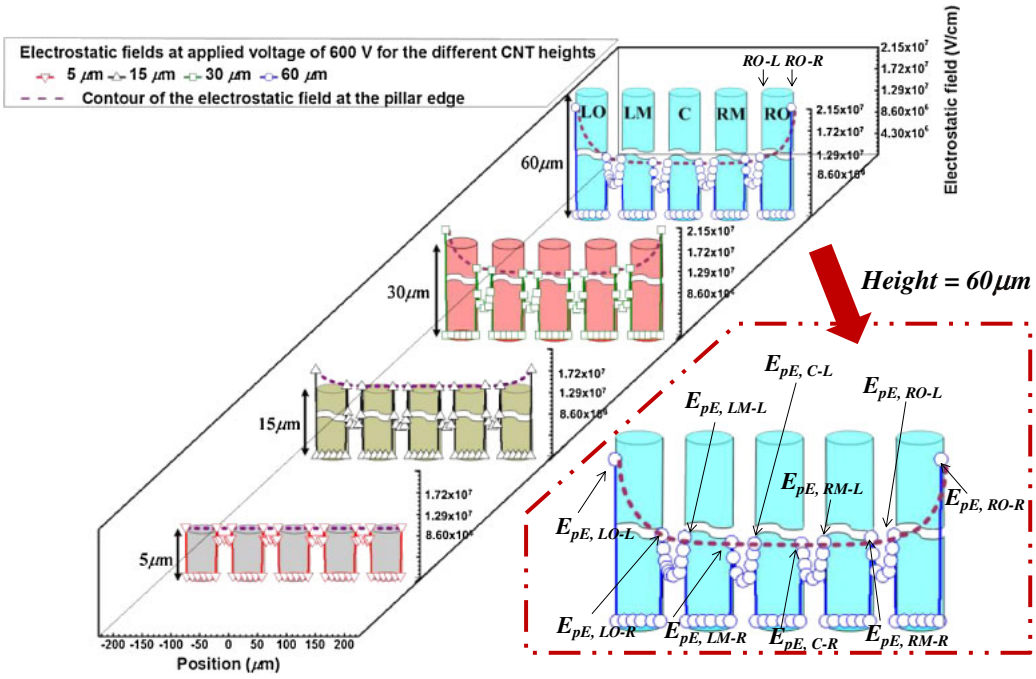

Fig. 5. (Color online) Electrostatic field distributions at applied voltage of 600 V and configurations of CNT pillars of different heights.

Table I. FE characteristics of CNTs of different pillar heights.

	Height (μm)				
	5	10	15	30	60
E_{to} (V/μm) at 10 μA/cm^2	1.22	1	0.84	1.07	1.12
E_{th} (V/μm) at 10 mA/cm^2	1.89	1.75	1.51	1.77	1.83

in the pillar. Similarly, the electrostatic fields between the pillars are smaller than those at the pillar edges owing to the field-screening effect (i.e., edge effect) caused by the proximity of neighboring CNT pillars. The phenomena can be found for all pillars with heights ranging from 5 to 60 μm. However, $E_{pE,LO\text{-}L}$ and the symmetrical $E_{pE,RO\text{-}R}$ increase linearly with increasing pillar height up to 15 μm and then tend to saturate at a pillar height of 60 μm, as shown in Fig. 6(a).

The electrostatic field distribution at the outermost CNTs of CNT pillars suffers from the minimum field-screening effect and edge effect. Therefore, the electrostatic field distribution at the outermost CNTs of CNT pillars depends on the height and radius of each CNT. In other words, $E_{pE,LO\text{-}L}$ and the symmetrical $E_{pE,RO\text{-}R}$ can be considered as the intrinsic electrical field at the outermost CNTs of CNT pillars and directly correlated with the intrinsic field enhancement factor β_0, which can be approximated as[24)]

$$\beta_0 = 1.2(H/r + 2.15)^{0.9} \text{ and } 4 \leq H/r \leq 3000, \quad (1)$$

where H and r are the height and radius of a CNT, respectively. In this study, the radius of a CNT is 8 nm and the H/r ratio changes from 625 to 1875 for pillar heights from 5 to 15 μm. Therefore, $E_{pE,LO\text{-}L}$ and the symmetrical $E_{pE,RO\text{-}R}$ increase as functions of pillar height. When the pillar height is larger than 24 μm, that is, the H/r ratio of the CNT exceeds 3000, both $E_{pE,LO\text{-}L}$ and the symmetrical $E_{pE,RO\text{-}R}$ tend to saturate, which can be explained as the

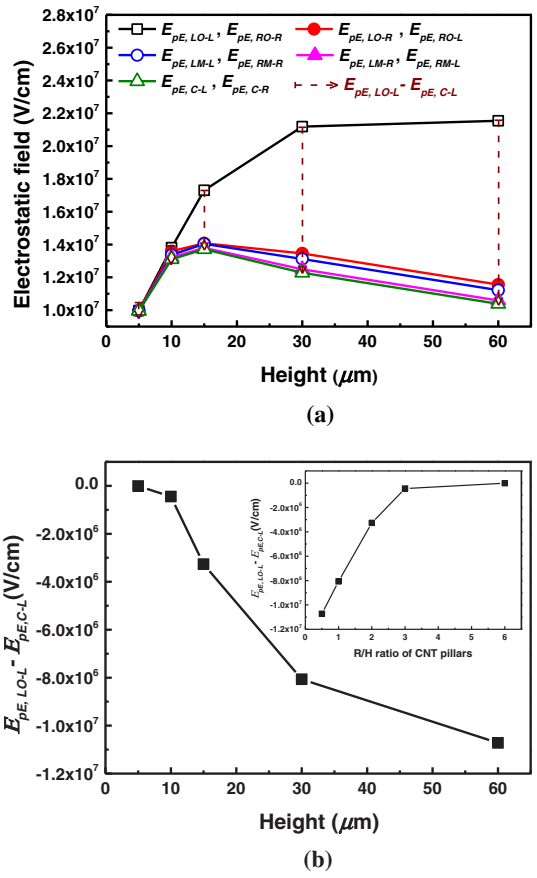

Fig. 6. (Color online) (a) Electrostatic field at each pillar edge at applied voltage of 600 V as a function of tube height obtained via computer simulation. (b) Difference between $E_{pE,C\text{-}L}$ and $E_{pE,LO\text{-}L}$ at applied voltage of 600 V as a function of tube height obtained via computer simulation. (The inset shows the difference between $E_{pE,C\text{-}L}$ and $E_{pE,LO\text{-}L}$ at an applied voltage of 600 V as a function of the R/H ratio.)

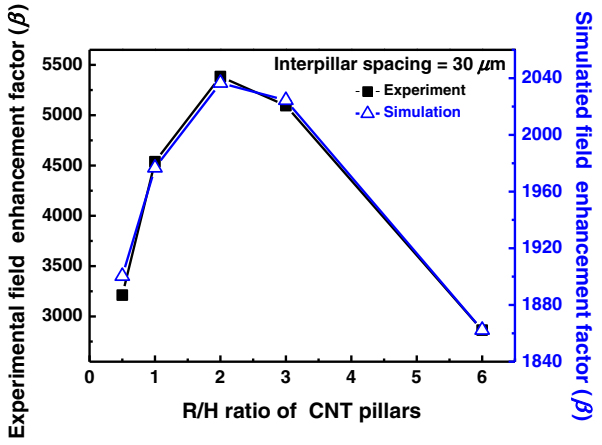

Fig. 7. (Color online) Field enhancement factors in experimental and simulation results as functions of R/H ratio.

equipotential curvature of a CNT being large enough to saturate with further increases in the CNT height. In contrast, the electrostatic fields at the pillar edges shown in Fig. 5, other than those of the outermost positions (i.e., $E_{pE,LO\text{-}L}$ and $E_{pE,RO\text{-}R}$), all increase as the pillar height increases from 5 to 15 μm and then decrease for pillar heights between 30 and 60 μm, as shown in Fig. 6(a). When the pillar height is less than 10 μm, the electrostatic fields at the pillar edges all increase with increasing pillar height. However, the field-screening effect is markedly intensified with increasing pillar height above 10 μm, causing the electrostatic fields at the pillar edges, other than those of the outermost positions (i.e., $E_{pE,LO\text{-}L}$ and $E_{pE,RO\text{-}R}$) to peak at a pillar height of 15 μm and then decrease with further increasing pillar height. Hence, the difference between $E_{pE,C\text{-}L}$ and $E_{pE,LO\text{-}L}$ (or that between the symmetrical $E_{pE,C\text{-}R}$ and symmetrical $E_{pE,RO\text{-}R}$) can be an index of the field-screening effect. Figure 6(b) shows the difference between $E_{pE,C\text{-}L}$ and $E_{pE,LO\text{-}L}$ as a function of the pillar height to reveal the field-screening effect of the interpillars. As shown in Fig. 6(b), the difference between $E_{pE,C\text{-}L}$ and $E_{pE,LO\text{-}L}$ is approximately constant when the pillar height is less than 10 μm and then decreases significantly when the pillar height increases from 15 to 60 μm, reflecting that the field-screening effect is markedly increased when the pillar height exceeds 10 μm. Furthermore, the inset of Fig. 6(b) shows the difference between $E_{pE,C\text{-}L}$ and $E_{pE,LO\text{-}L}$ as a function of the R/H ratio for CNT pillars. Clearly, the difference between $E_{pE,C\text{-}L}$ and $E_{pE,LO\text{-}L}$ decreases with increasing R/H ratio when the R/H ratio is less than 3 and tends to zero when the R/H ratio exceeds 3, indicating that the field-screening effect of the interpillars becomes negligible when the R/H ratio is larger than three.

Subsequently, the experimental results are compared with the simulation results. According to the FN mechanism, the emission current density J is calculated using[25)]

$$J = AE^2 \exp\left(-\frac{B}{E}\right), \tag{2}$$

where A and B are the FN constants dependent on the work function ϕ of the material. The simulated electrostatic field distributions of CNT pillars for the five different heights can be substituted into Eq. (2) to obtain the emission current density. In general,[12)] the material parameters for a CNT can be set as follows: band gap $E_g = 0.38$ eV, electron affinity $= 4.35$ eV, electron effective mass $m_e = 0.037m_0$, work function $\phi = 4.57$ eV, $A = 3.3698 \times 10^{-7}$ A/V^2, and $B = 6.6726 \times 10^8$ V/cm. By substituting the relation of $E = \beta E_m$ into Eq. (2), where E_m is the macroscopic field between electrodes and β is the field enhancement factor, which depends on the geometry of the device, the field enhancement factors β of CNT pillars of different heights can be extracted from the slopes of the FN plots. The field enhancement factors for the experimental results were extracted from the slopes of the FN plots in Fig. 4(b) by assuming a CNT work function of 4.57 eV. Both simulated and experimental field enhancement factors are shown together in Fig. 7 for comparison. The experimental relation between β and the R/H ratio is very consistent with the simulated results. Both exhibit a maximum field enhancement factor at an R/H ratio of two. The lower β values obtained by simulation can be attributed to the fact that only five pillars were considered in the simulation.

According to the results in Fig. 6(a), the electrostatic fields at the pillar edges, other than those of the outermost positions (i.e., $E_{pE,LO\text{-}L}$ and $E_{pE,RO\text{-}R}$) all peak at a CNT height of 15 μm. Since the electrostatic fields at the pillar edges, other than those of the outermost positions (i.e.,

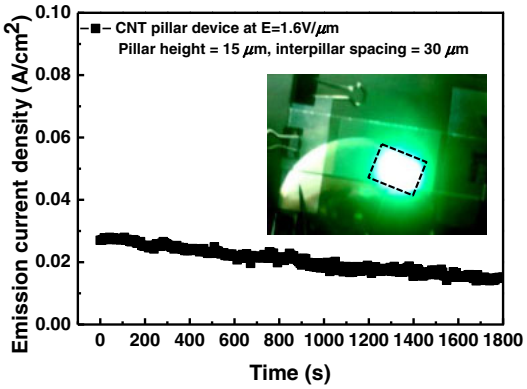

Fig. 8. (Color online) Current density as function of stress time and luminescent image at electric field of 1.6 V/μm over 1800 s at R/H ratio of 2.

$E_{pE,LO-L}$ and $E_{pE,RO-R}$) contribute most of the FE current densities for the CNT pillars, the current densities will also peak at a pillar height of 15 μm. Consequently, the field enhancement factors are maximum at an R/H ratio of 2 because the interpillar spacing R is 30 μm.

For the application of CNTs to FE devices, not only low-voltage emission but also emission uniformity in CNT films is critical. Therefore, the optimal CNT pillar, which has a height of 15 μm and an interpillar spacing of 30 μm, is stressed under an electric field of 1.6 V/μm for 1800 s. The current density as a function of the stress time and a luminescent image are shown in Fig. 8. From the figure, the fluctuations in the current density and percentage of emission area are about 17 and 95% over 1800 s, respectively. The optimal CNT pillar has a highly uniform emission area and a high current density owing to the uniform length of the CNT synthesized using the Co–Ti/Ti codeposited catalyst layer and the better adhesion between the CNT and substrate.[22)]

4. Conclusions

Optimal FE properties, including a high field enhancement factor β of 5384 and a low turn-on field E_{to} of 0.84 V/μm at a current density = 10 μA/cm^2, have been achieved via the use of vertically aligned CNT pillars with a height of 15 μm and an interpillar spacing of 30 μm. For an R/H ratio larger than two, β increases with increasing pillar height since the fields are enhanced by increasing the aspect ratio. However, β decreases with increasing pillar height owing to the enhanced field-screening effect for an R/H ratio less than two. A simulation has also been performed to verify the experimental results. The results obtained in this study can serve as useful references when designing high-efficiency field-emission CNTs for application in displays and sensors.

Acknowledgments

This research was financially supported by the National Science Council of Taiwan under Contract No. NSC 99-2221-168-MY3. The authors would like to thank the Nano Facility Center (NFC) of National Chiao Tung University and the National Nano Device Laboratories (NDL) for their technical support.

1) S. H. Jo, Y. Tu, Z. P. Huang, D. L. Carnahan, D. Z. Wang, and Z. F. Ren: Appl. Phys. Lett. **82** (2003) 3520.
2) O. Gröning, O. M. Küttel, Ch. Emmenegger, P. Gröning, and L. Schlapbach: J. Vac. Sci. Technol. B **18** (2000) 665.
3) L. Nilsson, O. Groening, C. Emmenegger, O. Kuettel, E. Schaller, L. Schlapbach, H. Kind, J-M. Bonard, and K. Kern: Appl. Phys. Lett. **76** (2000) 2071.
4) J.-M. Bonard, N. Weiss, H. Kind, T. Stöckli, L. Forró, K. Kern, and A. Châtelain: Adv. Mater. **13** (2001) 184.
5) M. Chhowalla, C. Ducati, N. L. Rupesinghe, K. B. K. Teo, and G. A. J. Amaratunga: Appl. Phys. Lett. **79** (2001) 2079.
6) K. B. K. Teo, M. Chhowalla, G. A. J. Amaratunga, W. I. Milne, G. Pirio, P. Legagneux, F. Wyczisk, D. Pribat, and D. G. Hasko: Appl. Phys. Lett. **80** (2002) 2011.
7) J. S. Suh, K. S. Jeong, J. S. Lee, and I. Han: Appl. Phys. Lett. **80** (2002) 2392.
8) J.-M. Bonard, F. Maier, T. Stöckli, A. Châtelain, W. A. de Heer, J.-P. Salvetat, and L. Forró: Ultramicroscopy **73** (1998) 7.
9) J.-M. Bonard, M. Croci, I. Arfaoui, O. Noury, D. Sarangi, and A. Châtelain: Diamond Relat. Mater. **11** (2002) 763.
10) R. C. Smith and S. R. P. Silva: J. Appl. Phys. **106** (2009) 014314.
11) H. Liu and Y. Saito: J. Nanosci. Nanotechnol. **10** (2010) 3983.
12) S. Fujii, S. Honda, H. Machida, H. Kawai, K. Ishida, M. Katayama, H. Furuta, T. Hirao, and K. Oura: Appl. Phys. Lett. **90** (2007) 153108.
13) J. L. Killian, N. B. Zuckerman, D. L. Niemann, B. P. Ribaya, M. Rahman, R. Espinosa, M. Meyyappan, and C. V. Nguyen: J. Appl. Phys. **103** (2008) 064312.
14) L. Zhu, J. Xu, Y. Xiu, Y. Sun, D. W. Hess, and C. P. Wong: Carbon **44** (2006) 253.
15) T.-W. Weng, Y.-H. Lai, and K.-Y. Lee: Appl. Surf. Sci. **254** (2008) 7755.
16) J. L. Silan, D. L. Niemann, B. P. Ribaya, M. Rahman, M. Meyyappan, and C. V. Nguyen: Appl. Phys. Lett. **95** (2009) 133111.
17) P. Rai, D. R. Mohapatra, K. S. Hazra, D. S. Misra, and S. P. Tiwari: Appl. Phys. Lett. **93** (2008) 131921.
18) G.-H. Jeong, N. Olofsson, L. K. L. Falk, and E. E. B. Campbell: Carbon **47** (2009) 696.
19) H. M. Manohara, M. J. Bronikowski, M. Hoenk, B. D. Hunt, and P. H. Siegel: J. Vac. Sci. Technol. B **23** (2005) 157.
20) M. Katayama, K.-Y. Lee, S. Honda, T. Hirao, and K. Oura: Jpn. J. Appl. Phys. **43** (2004) L774.
21) S. Fujii, S. Honda, H. Kawai, K. Ishida, K. Oura, and M. Katayama: Diamond Relat. Mater. **17** (2008) 556.
22) H.-C. Cheng, K.-C. Lin, H.-C. Tai, C.-P. Juan, R.-L. Lai, Y.-S. Liu, H.-W. Chen, and Y.-Y. Syu: Jpn. J. Appl. Phys. **46** (2007) 4359.
23) H.-C. Cheng, R.-L. Lai, Y.-R. Chang, K.-C. Lin, C.-P. Juan, P.-C. Chang, C.-Y. Lee, and J.-K. Shiu: Jpn. J. Appl. Phys. **46** (2007) 863.
24) C. J. Edgcombe and U. Valdrè: J. Microsc. **203** (2001) 188.
25) Y.-C. Lan, M. X. Yan, and W.-J. Liu: J. Vac. Sci. Technol. B **25** (2007) 497.